NANO LETTERS

2008
Vol. 8, No. 5
1492-1500

Modulation of in Vivo Tumor Radiation Response via Gold Nanoshell-Mediated Vascular-Focused Hyperthermia: Characterizing an Integrated Antihypoxic and Localized Vascular Disrupting Targeting Strategy

Parmeswaran Diagaradjane,[‡] Anil Shetty,[§] James C. Wang,[‡,⊥] Andrew M. Elliott,[§] Jon Schwartz,[⊥] Shujun Shentu,[‡] Hee C. Park,[‡] Amit Deorukhkar,[‡] R. Jason Stafford,[§] Sang H. Cho,[†,||] James W. Tunnell,[#] John D. Hazle,[§] and Sunil Krishnan*[,‡]

Departments of Experimental Radiation Oncology, Imaging Physics, and Radiation Physics, The University of Texas M. D. Anderson Cancer Center, Houston, Texas, Nanospectra Biosciences Inc., Houston, Texas, Department of Biomedical Engineering, University of Texas at Austin, Austin, Texas

Received February 19, 2008; Revised Manuscript Received March 25, 2008

ABSTRACT

We report noninvasive modulation of in vivo tumor radiation response using gold nanoshells. Mild-temperature hyperthermia generated by near-infrared illumination of gold nanoshell-laden tumors, noninvasively quantified by magnetic resonance temperature imaging, causes an early increase in tumor perfusion that reduces the hypoxic fraction of tumors. A subsequent radiation dose induces vascular disruption with extensive tumor necrosis. Gold nanoshells sequestered in the perivascular space mediate these two *tumor vasculature-focused* effects to improve radiation response of tumors. This novel integrated antihypoxic and *localized* vascular disrupting therapy can potentially be combined with other conventional antitumor therapies.

Introduction. Gold nanoshells are a class of metal nanoparticles consisting of a silica core with a gold coating on the surface that are optically tunable over a broad region of the electromagnetic spectrum. The relative thickness of the core and gold layer of the nanoshell have been engineered such that their plasmon resonance upon illumination with near-infrared (NIR) light ($\lambda = 808$ nm) leads to intense absorption of light and conversion to thermal energy. When injected intravenously, gold nanoshells measuring 150 ± 10 nm accumulate preferentially in tumors by the enhanced permeability and retention (EPR) effect, where the leaky tumor vasculature containing wide interendothelial junctions, abundant transendothelial channels, incomplete or absent basement membranes, and dysfunctional lymphatics contribute to passive extravasation of systemically injected macromolecules and nanoparticles into tumors.[1–4] Gold nanoshells have been used in combination with a NIR laser for minimally invasive *thermal ablation* of tumor tissues.[5] Following this seminal report, several studies have been reported on the use of gold nanoshells for photothermal therapy,[6] molecular imaging at the cellular level,[7] NIR tissue welding,[8] contrast enhancement in optical coherence tomography,[9] and magnetic resonance imaging.[10] More recently, the kinetics and biodistribution of gold nanoshells in circulating blood and internal organs of mice has been reported.[11]

* Corresponding author. E-mail: skrishnan@mdanderson.org. Telephone: 713-563-2377. Fax: 713-563-2366. Address: Dr. Sunil Krishnan, The University of Texas M. D. Anderson Cancer Center, 1515 Holcombe Boulevard, Unit-97, Houston, Texas 77030.

† Current address: Nuclear/Radiological Engineering and Medical Physics Program, Georgia Institute of Technology, Atlanta, Georgia.

‡ Department of Experimental Radiation Oncology, The University of Texas M. D. Anderson Cancer Center.

§ Department of Imaging Physics, The University of Texas M. D. Anderson Cancer Center.

|| Department of Radiation Physics, The University of Texas M. D. Anderson Cancer Center.

⊥ Nanospectra Biosciences Inc.

Department of Biomedical Engineering, University of Texas at Austin.

10.1021/nl080496z CCC: $40.75
Published on Web 04/16/2008

Although extensive preclinical reports are available on the utility of gold nanoshells alone for diagnostic and therapeutic applications, we are unaware of any reports documenting their utility as an adjuvant therapeutic strategy to improve the efficacy of the currently available clinical therapeutic modalities, in particular, radiation therapy.

Radiation therapy is an essential component of the multidisciplinary approach to the treatment of many tumors. However, as a single modality, radiation therapy is unable to eradicate all locoregional recurrences and/or cure localized cancers. This is largely related to the intrinsic resistance of some cancer cells to ionizing radiation.[12] Intratumoral hypoxia is a key mediator of this resistance to radiation therapy and is secondary to inadequate oxygenation via mutated, chaotic, and incomplete blood vessels in tumors.[13,14] Hypoxia is known to induce the expression of a spectrum of genes involved in metabolism, proliferation, apoptosis, and angiogenesis.[15,16] These hypoxia-induced tumor cellular and microenvironmental changes contribute to tumor aggressiveness and resistance to radiation therapy.[17] Consequently, any therapeutic strategy that alleviates tissue hypoxia could potentially overcome a major mechanism of radioresistance and enhance the effects of radiation therapy. One such highly effective therapeutic adjunct to radiation therapy is mild temperature hyperthermia, which has direct antitumor effects and tumor microenvironment effects mediated, in part, through mitigation of hypoxia, that contribute to the observed radiosensitization.[18–20] Mild temperature hyperthermia mediates its antitumor effects via subtle influences on the tumor microenvironment, activation of immunological processes, induction of gene expression, and induction of protein synthesis.[20] While these effects do not independently cause tumor cell cytotoxicity, they lead to greater effectiveness of other conventional treatment modalities such as radiation therapy, chemotherapy, and immunotherapy. In particular, in its role as an adjunct to radiation therapy, hyperthermia serves as a dose-modifying agent that increases the therapeutic ratio of radiation therapy (i.e., enhanced effectiveness of a given dose of radiation therapy without additional toxicity). Several randomized trials have demonstrated improved response rates and survival when patients with locally advanced malignancies are treated with locoregional hyperthermia and radiotherapy compared to radiotherapy alone. Despite convincing evidence for hyperthermic radiosensitization, it is underutilized in routine clinical practice for the following reasons: (a) the invasive means of achieving and maintaining hyperthermia, (b) the time commitment involved in a treatment that lasts about an hour, (c) the lack of good thermal dosimetry, and (d) the inability to achieve localized hyperthermic temperatures.[21] A noninvasive method to generate and monitor hyperthermia would provide renewed enthusiasm for such treatments. A potentially novel and minimally invasive method to induce mild temperature hyperthermia treatment is to use optically activated gold nanoshells.

In this investigation we demonstrate modulation of in vivo tumor radiation response using gold nanoshell-mediated hyperthermia via a dual vascular-focused mechanism: (a) an early increase in perfusion that reduces the radioresistant hypoxic fraction of tumors and (b) a subsequent induction of vascular disruption/collapse and extensive necrosis that complements radiation-induced cell death. These *tumor vasculature-focused* effects mediated by perivascularly sequestered gold nanoshells characterize a novel and integrated antihypoxic and *localized* vascular disrupting therapeutic strategy.

Gold Nanoshell Distribution in Tumor Tissues. Gold nanoshells were fabricated using colloidal silica (120 ± 12 nm diameter) as the core material (Precision Colloids, LLC, Cartersville, GA). Gold colloids $\sim 1-3$ nm in diameter were grown by using the method of Duff[22] and aged for 2 weeks at 4 °C, after which the aged gold colloid suspension was mixed with aminated silica particles. Gold colloid adsorbs to the amine groups on the surface of the silica core to form nucleating sites, which were further reacted with $HAuCl_4$ in the presence of formaldehyde. This process reduces additional gold onto the adsorbed colloid, which acts as a nucleation site, causing the surface colloid to grow and coalesce with a neighboring gold colloid, forming a complete metal shell. Particles were designed to have a 120 nm core diameter and a 12−15 nm thick shell, resulting in an optical absorption peak between 780 and 800 nm (Figure 1a), assessed by UV−vis spectrophotometry. Thiolated polyethylene glycol (SH-PEG) (Laysan Bio, Huntsville, AL) was assembled onto nanoshell surfaces by combining 5 μM SH-PEG and nanoshells in DI H_2O for 12 h, followed by diafiltration to remove the excess SH-PEG. The resulting nanoshells were coated with an average of 3.2×10^5 SH-PEG molecules and suspended in 10% trehalose solution to create an iso-osmotic solution for injection.

Localized Mild-Temperature Hyperthermia Can Be Induced Noninvasively by Optically Activated Gold Nanoshells and Measured Noninvasively by Magnetic Resonance Temperature Imaging (MRTI). To optimize the laser settings for generation of mild-temperature hyperthermia over a short period of time without significant overheating of both tumor and/or surrounding normal tissues, we initially recorded temperature increases under different laser illumination conditions in an in vivo tumor model using tumor-implanted thermocouples. Six- to eight-week-old immunocompromised male nude (Swiss nu/nu) mice weighing 20−25 g each (purchased from our in-house specific pathogen-free breeding colony) were subcutaneously inoculated with human colorectal cancer cells (HCT 116; $\sim 2 \times 10^6$ cells per 50 μL of sterile phosphate buffered saline) into the right thigh. When the tumors attained a size of ~7−8 mm in diameter, $\sim 8 \times 10^8$ nanoshells/g body weight were directly injected into the tail vein. Localized hyperthermia was carried out 20−24 h postinjection. Needle thermocouples (HYP1-30-1/2-T-G-60-SMP-M, Omega Engineering) were positioned into the tumor core and at the tumor base (adjacent to the muscular fascia). Core body temperature was measured via rectal thermometer (RET-3, Braintree Scientific, Inc.). Three different laser settings were evaluated: 0.8, 0.6, and 0.4 W in cohorts of 2−3 mice each. Prior to laser illumination PEG diacrylate (M_x 600, Sartomer, West Chester, PA)

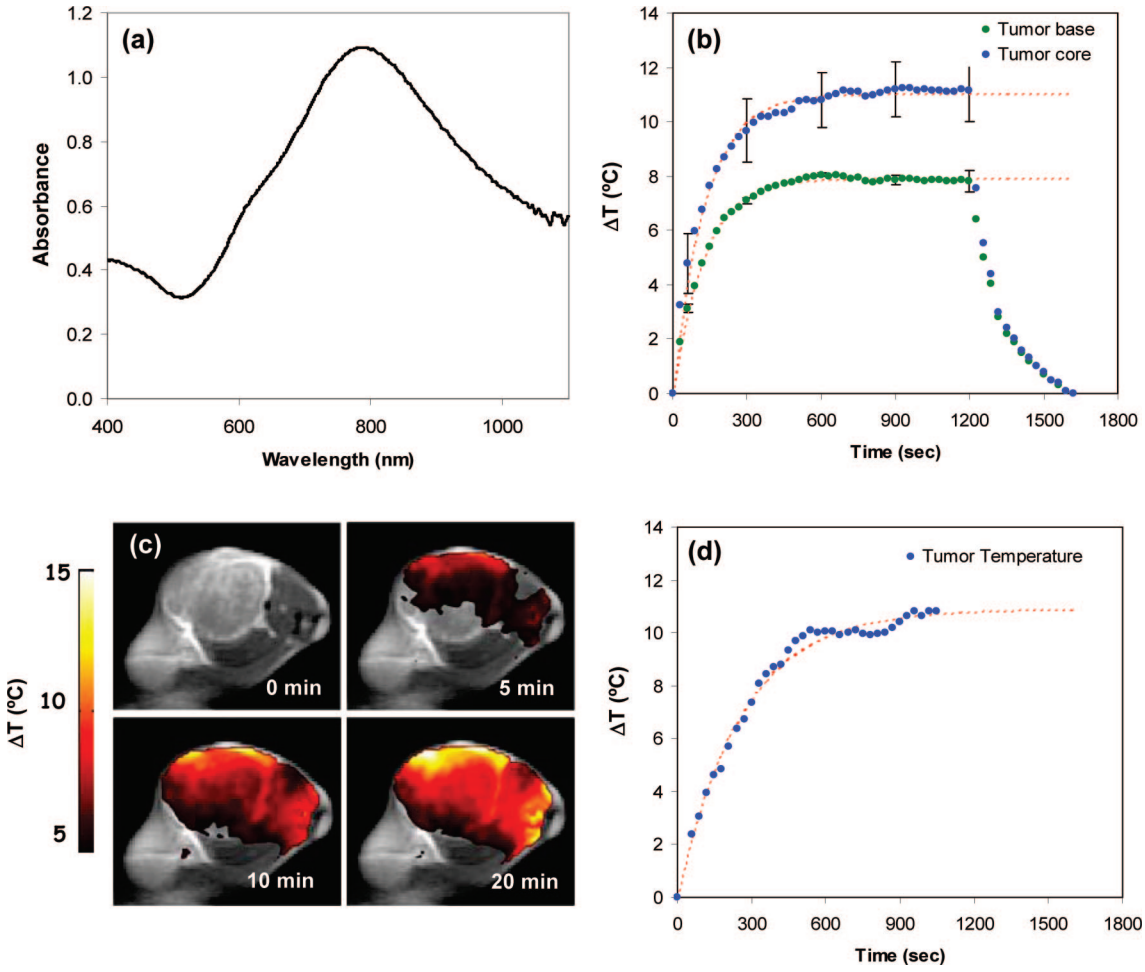

Figure 1. (a) Absorption spectra of gold nanoshells (silica core diam: 120 ± 12 nm; gold shell diam: 12 ± 3 nm), (b) temperature profile of tumor tissue measured by thermocouples, (c) MRTI images of tumor tissues at various time periods, and (d) temperature profile in tumor tissue estimated from the MRTI at various time points during laser illumination at ~24 h after gold nanoshell injection. The red dotted line in (c) and (d) represents the best-fit line.

was applied over the surface of the tumor as an index-matching agent. An 808 nm diode laser (Diomed 15-plus, Diomed, Inc., Cambridge UK) was used to illuminate the tumor surface (10 mm diameter spot size) via a fiber optic cable with a collimating lens. Average baseline tumor temperature was ~30 ± 1 °C. Upon illumination with a laser power setting of 0.8 W, a steep rise in tumor temperature was observed over the first 5 min, followed by a steady temperature plateau (ΔT of ~13−15 °C) for the remaining 15 min of laser illumination, which was still below the typical hyperthermia temperature threshold (<45 °C). Because our intent was to generate mild-temperature hyperthermia without inducing tissue damage by the hyperthermia itself, we chose a lower power setting. Irradiation with a laser power setting of 0.4 W achieved a ΔT of 4−5 °C in the tumor core, which was considered to be insufficient. An intermediate laser power setting of 0.6 W, yielded ΔTs of ~10 ± 1.5 °C and ~8 ± 0.5 °C in the tumor core and base, respectively (Figure 1b). These irradiation parameters [λ = 808 nm, power setting = 0.6 W, 75% duty factor, average optical irradiance = 350 mW/cm^2 at a spot size of 10 mm (0.78 cm^2)] were verified for reproducibility in an additional cohort of mice and then chosen for all subsequent hyperthermia experiments. The observed differences in temperature between the tumor core and base were attributable to (a) the limitation in depth of penetration of the NIR laser beam within tumor tissues, (b) the absorption of NIR light by the gold nanoshells in the superficial layers of the tissues, and (c) the preferential accumulation of and absorption of NIR light by gold nanoshells within the perivascular space of blood vessels lining the periphery of the tumor. To further confirm that the induced temperature rise was mediated by gold nanoshells, temperature measurements were undertaken using identical laser settings in a cohort of control animals without nanoshells. ΔTs of ~ 2.5−3.5 °C were observed in the tumor core, the base of the tumor, and in irradiated muscle of the contralateral thigh.

The thermocouple measurements were subsequently validated by noninvasive in vivo MRTI[23] in an additional cohort of mice (see Supporting Information for details). Upon laser illumination with a power of 0.6 W, real-time MRTI measurements demonstrated a temperature difference (ΔT) of ~11.0 °C consistent with the thermocouple measurements. The T1-weighted images overlaid with the temperature distribution images at 0, 5, 10, and 20 min after laser illumination are illustrated in Figure 1c. The ΔT of

~15.0 °C observed in the tumor periphery (MRTI) may be attributable to the high concentration of nanoshells within the highly vascularized tumor periphery. Regions of interest (ROIs) encompassing the whole tumor, tumor periphery, and tumor core were created and averaged to generate temperature plots at various time points. A similar ROI from the background region was selected to compensate for background temperature changes. The temperature rise calculated from the real-time MRTI measurements is illustrated in Figure 1d. Similar to the thermocouple measurements, an initial steep rise in temperature was followed by a relatively sustained plateau region for the remaining period of laser illumination. However, the slope of the initial temperature rise was different from that of the thermocouple measurements, possibly attributable to the averaging of temperature across a larger ROI in the MRTI measurements as opposed to point measurements obtained from the thermocouple.

Gold Nanoshell-Mediated Hyperthermia Enhances the Efficacy of Radiation Therapy. In a separate experiment employing the tumor regrowth delay assay, 36 mice bearing ~7−8 mm diameter tumors were evenly randomized to one of four treatment conditions: (a) control treatment with gold nanoshells alone without hyperthermia or radiation, (b) 20 min of laser illumination as specified above for generation of mild-temperature hyperthermia, (c) a single 10 Gy dose of radiation therapy using 125 kV X-rays (Phillips RT-250 orthovoltage X-ray unit operated at 20 mA and using a 2 mm aluminum filter and a skin cone of 1 cm diameter to collimate the beam to the tumor surface with the target-to-surface distance of 22.4 cm; see Supporting Information for experimental setup), and (d) hyperthermia followed by 10 Gy radiation therapy (thermoradiotherapy) ~3−5 min later. Tumor growth was followed by serially measuring tumor dimensions in two orthogonal directions (long axis: a_1; short axis: a_2) twice weekly. Tumor volume was calculated using the expression $(\pi/6)\cdot(a_1)\cdot(a_2)^2$ and plotted over time as represented in Figure 2a. The tumor volume of individual mice in each treatment group was normalized with respect to the initial tumor volume prior to treatment. Tumor regrowth delays, calculated as the time to doubling of tumor volume, were observed to be approximately 4, 9, 17, and 29 days for the control, hyperthermia, radiation, and thermoradiotherapy groups, respectively. As illustrated in Figure 2b, there was a statistically significant ($p < 0.005$) difference in tumor doubling time between the radiation and thermoradiotherapy groups.

Gold Nanoshell-Mediated Hyperthermia Enhances Perfusion. Because one of the purported mechanisms of radiosensitization by mild-temperature hyperthermia is an acute increase in tumor vascular perfusion, we used dynamic contrast enhanced magnetic resonance imaging (DCE-MRI) to evaluate contrast uptake in tumors following treatment. Approximately 3−5 min after the completion of laser illumination at standard settings, DCE-MRI was performed in a separate cohort of mice (see Supporting Information for details). Representative precontrast MRI images and pre- and posthyperthermia T1-weighted DCE-MRI images are illustrated in Figure 3a−c. The baseline prehyperthermia DCE-MRI image (Figure 3b) revealed contrast enhancement at the periphery of the tumor with relative paucity of contrast in the tumor core. After laser illumination, a significant increase in contrast was observed within the tumor core (Figure 3c). This increase in contrast within the tumor core is further illustrated by a 3D pixel intensity representation of a ROI (34 × 37 pixels) encompassing the entire tumor in Figure 3d−f. Prehyperthermia contrast-enhanced images demonstrated higher pixel intensity values near the tumor periphery, whereas the immediate posthyperthermia contrast-enhanced images demonstrated an approximately 50% increase in pixel intensity value in the tumor core (Figure 3f) as compared to the prehyperthermia images (Figure 3e). The contrast uptake before and after gold nanoshell-mediated hyperthermia in the tumor core and in the whole tumor is further illustrated in Figure 3g,h. The slopes (mean ± SE) of the pre- and posthyperthermia contrast uptake in the tumor core were estimated as 2.49 ± 0.51 and 4.38 ± 0.60 arbitrary units (a.u.)/s, respectively, and the corresponding values for

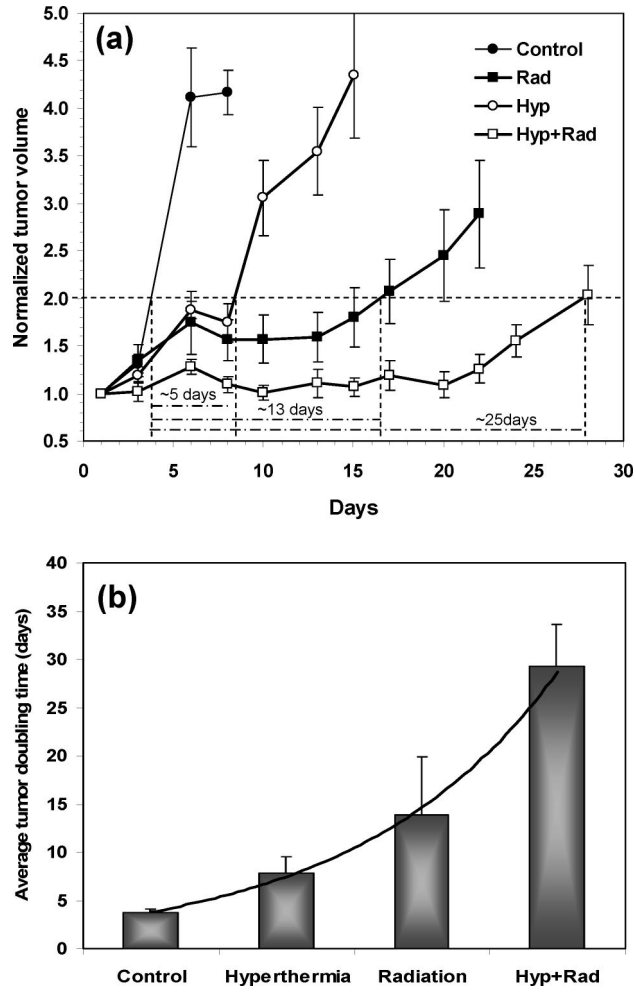

Figure 2. (a) Normalized tumor volume plot of control, hyperthermia, radiation, and thermoradiotherapy groups showing the mean ± SE values at different time periods after the initiation of each treatment and (b) the corresponding tumor doubling time after each treatment.

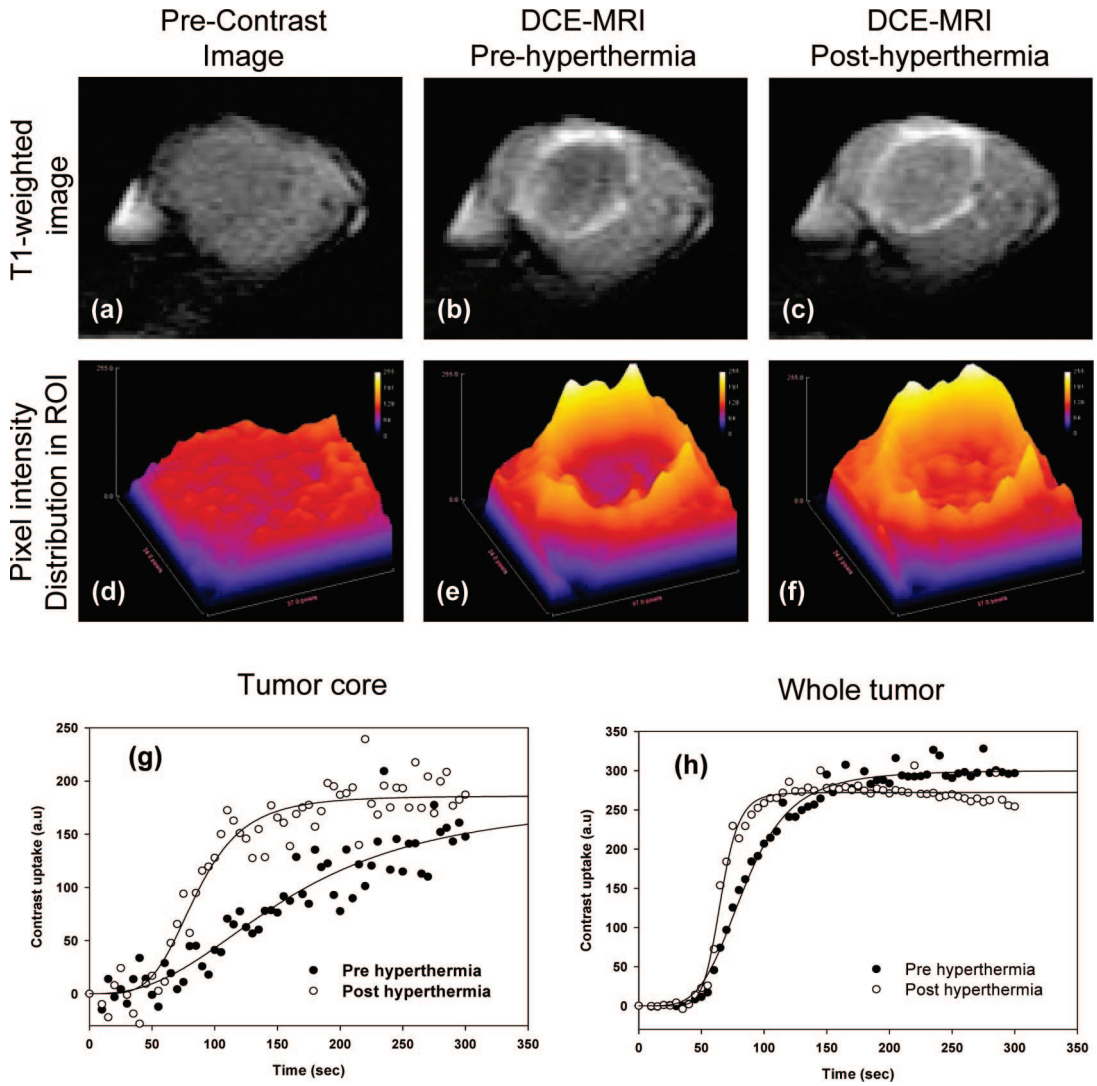

Figure 3. T1-weighted (a) precontrast, (b) prehyperthermia DCE-MRI, (c) posthyperthermia DCE-MRI images of tumor, and (d−f) the corresponding 3D pixel intensity distribution profile. Enhanced contrast (bright tumor center) observed in posthyperthermia DCE-MRI when compared to prehyperthermia shows increased perfusion after gold nanoshell-mediated hyperthermia. Pre- and posthyperthermia contrast uptake estimated from the ROI encompassing the tumor core and whole tumor is illustrated in (g) and (h), respectively.

the whole tumor were 4.42 ± 0.22 and 8.99 ± 0.69 au/s, respectively.

Ex Vivo Analysis of Tumor Tissue. Two mice from each group were euthanized 90 min after all treatments and tumors were extracted for ex vivo analyses. Hematoxylin and eosin (H and E) staining of the peripheral and core regions of tumors from all four treatment groups is illustrated in Figure 4a−h, with arrows representing the necrotic regions. No necrotic regions were observed in the tumor periphery of control, hyperthermia, and radiation groups (Figure 4a−c), respectively. However, necrotic regions were observed at a distance of ∼1.4 mm from the tumor periphery in the thermoradiotherapy group (Figure 4d). The tumor core of control, hyperthermia, and radiation groups demonstrated small necrotic regions in the range of ∼0.17−0.4 mm (Figure 4e−g), respectively. In contrast to these small necrotic regions, large necrotic regions in the range of ∼0.6−1.2 mm were observed in the tumor core of the thermoradiotherapy group (Figure 4h).

Markers for Tissue Hypoxia, Blood Flow, and Proliferation. To further understand the mechanism of extensive necrosis noted on H and E staining, we evaluated these tumor specimens from all four groups for changes in tumor cell proliferation as well as changes in the tumor microenvironment, specifically with assessment of hypoxia and blood flow (see Supporting Information for marker injection and immunofluorescence staining procedure). The hypoxic (green) and proliferative (red) regions in control, hyperthermia, radiation, and thermoradiotherapy groups are represented in parts a−d of Figure 5, respectively. In the control and radiation groups, the hypoxic regions were predominantly in the tumor core, while the proliferative regions were largely confined to the periphery of the tumor. However, in the hyperthermia group (Figure 5b), the proliferative regions extended to the tumor core with a corresponding decrease in the hypoxic area in the tumor core. This may be attributable to the increased vascular perfusion induced by gold nanoshell-mediated hyperthermia. Higher magnification

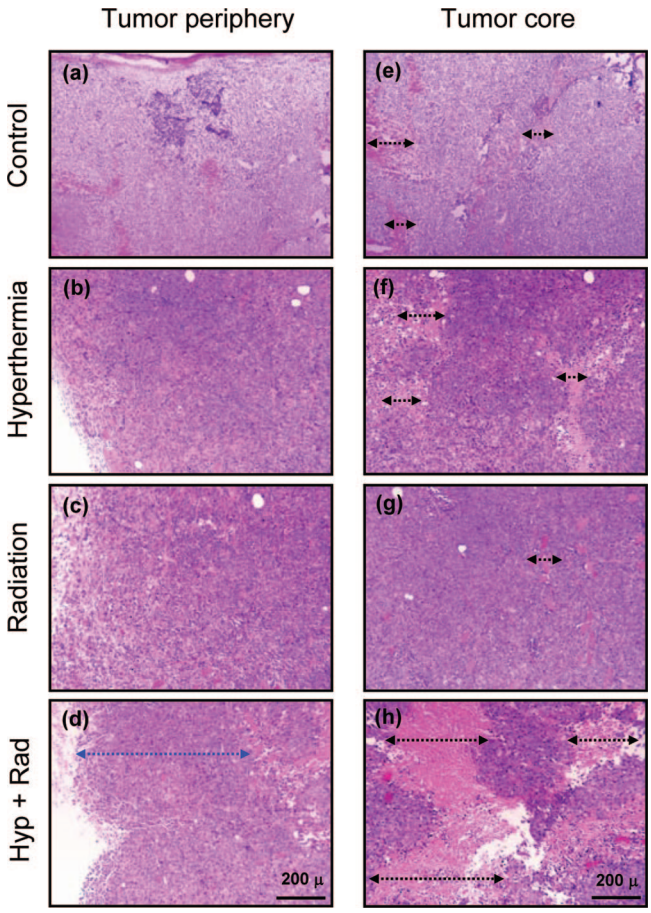

Figure 4. H and E staining of tumor (a−d) periphery and (e−h) core, tissues from control, hyperthermia, radiation, and thermoradiotherapy treated groups. The black arrows in (e−h) represents the regions of necrosis in the tumor center and the blue arrow in (d) represents the depth of necrosis from the tumor periphery. Representative scale bar is shown in the bottom image of each column.

images of the periphery and tumor core of different treatment groups demonstrating blood perfusion (blue) and tissue hypoxia (green) are shown in parts e−h and i−l of Figure 5, respectively. Regions of blood flow (blue) are associated with scant tissue hypoxia (green). At higher magnification, more distinct differences in the patterns of the hypoxic region were observed between the thermoradiotherapy and other groups. The control, hyperthermia, and radiation groups demonstrated a structured pattern of a hypoxic region in the tumor core with regions of perfusion between the hypoxic regions (Figure 5i−k). In contrast to this, the thermoradiotherapy group demonstrated a distortion of this architecture characterized by patchy hypoxic regions with no distinct regions of blood flow in the tumor core (Figure 5l). We hypothesized that this was a reflection of a hindrance to perfusion that also explains the massive necrosis observed on H and E staining.

Assessment of Tumor Microvessels. To evaluate the pattern of tumor vasculature in all four groups, we performed CD31-immunofluorescence staining on all tumors extracted 90 min following treatments (Figure 6a). No significant difference in the microvessel density was observed between the control, hyperthermia, and radiation groups. However, the microvessel density was significantly lower ($p < 0.05$) in the thermoradiotherapy group compared to other groups. The differences in microvessel density in the tumor periphery and the tumor core of all groups illustrated in Figure 6b confirm the relative scarcity of microvessels in tumors treated with thermoradiotherapy. Therefore, our results indicate that thermoradiotherapy leads to an acute increase in perfusion of tumors immediately following hyperthermia (as demonstrated by DCE-MRI 3−5 min following hyperthermia) and a subsequent distortion of vascular patterns (as demonstrated by the decrease in microvessel density 90 min following radiation). We hypothesized that these observations are best explained by the nature of hyperthermia induced by gold nanoshells wherein focal temperature rises are much more pronounced adjacent to the nanoshells as compared to further away, thereby creating heterogeneity in the distribution of temperature within the entire tumor. Because this heterogeneity, with sharp temperature gradients around the nanoshells, may contribute to the observed vascular pattern disruption, we determined the precise location of gold nanoshells within tumors in the control and hyperthermia groups.

Localization of Gold Nanoshells within the Tumor Microenvironment. The microscopic distribution of gold nanoshells in tumors was determined by scanning electron microscopy (SEM). SEM was performed using a JSM-5910 scanning electron microscope operating at an accelerating voltage of 15 kV (JEOL, USA, Inc., Peabody, MA). In control tumors, SEM images revealed predominant accumulation/ distribution of nanoshells in perivascular regions (represented by white arrows) in the tumor tissues (Figure 6c, row 1). Similarly, in the hyperthermia group, SEM images (Figure 6c, row 2) revealed intact blood vessels with nanoshells distributed in the perivascular region. Taken together, we hypothesize that this perivascular sequestration of gold nanoshells leads to a focal temperature rise near the blood vessels after hyperthermia, which, in turn, leads to (i) an acute increase in perfusion (Figure 3) and (ii) a greater focal sensitivity to subsequent radiation that results in vascular disruption (Figure 5l).

Our results indicate that hyperthermia mediated by gold nanoshells uniquely improves the efficacy of radiation therapy by two mechanisms: (a) an early increase in perfusion that reduces the fraction of hypoxic cells that contribute to radiation resistance and (b) a subsequent (∼90 min after treatment) induction of vascular disruption/collapse and extensive necrosis that complements radiation-induced cell death. This unique dual effect of gold nanoshell-mediated hyperthermia is a consequence of the focal temperature rise generated adjacent to tumor vasculature where nanoshells have sequestered preferentially. The first mechanism of observed improvement in the efficacy of radiation therapy was due to the increased vascular perfusion of the tumor. Tumors are typically perfused by a network of morphologically and functionally abnormal vessels recruited by an orchestrated series of dynamic events (angiogenesis) driven by the increasing demand for oxygen and nutrients by proliferating tumor cells.[24,25] The resulting temporal and spatial heterogeneity of blood flow leads to distinct regions

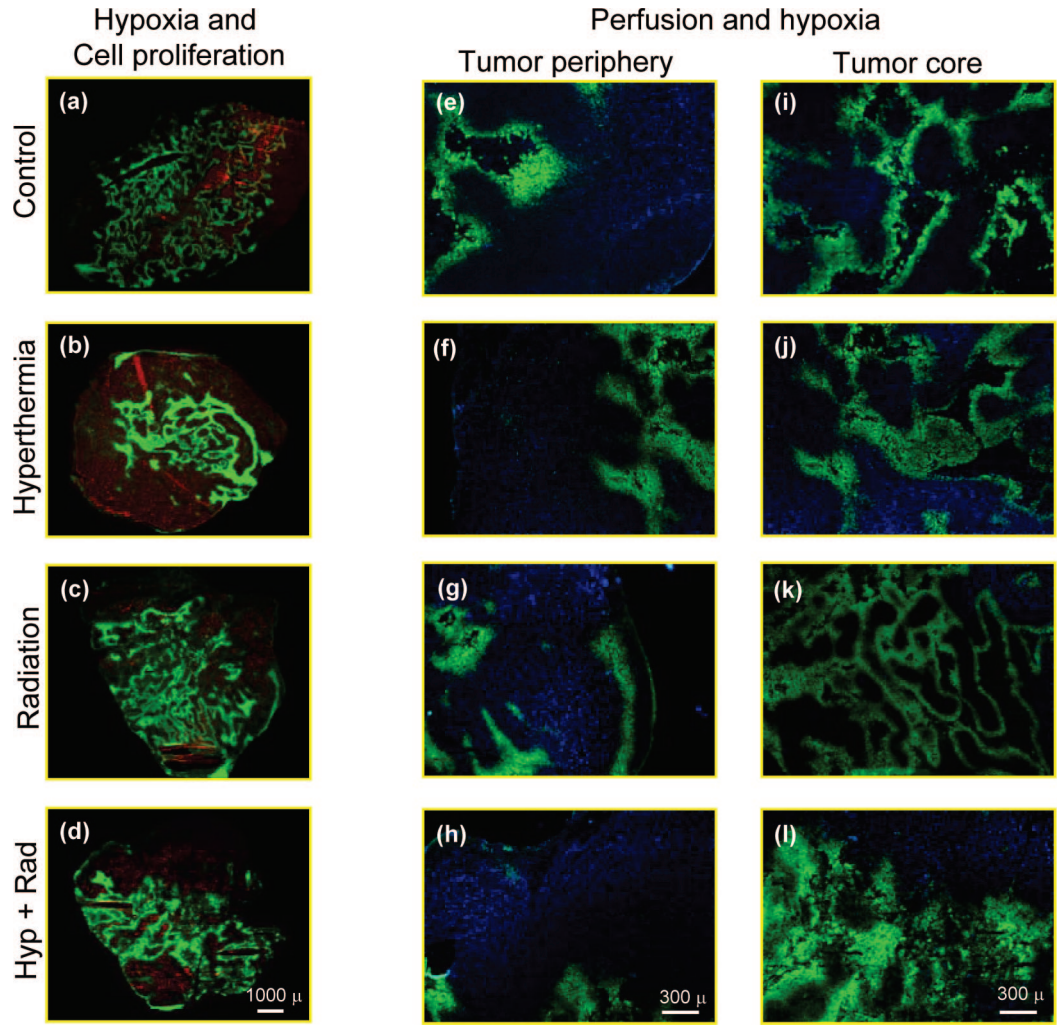

Figure 5. Immunofluorescence staining of control, hyperthermia, radiation, and thermoradiotherapy treated tumors showing hypoxia, cell proliferation (a−d), and hypoxia, perfusion in tumor periphery (e−h), and tumor core (i−l), respectively. Red, blue, and green fluorescence represents cell proliferation, perfusion, and hypoxic regions in tumors. Patchy hypoxic region seen in (l) is attributed to the vascular disruption effect induced by gold nanoshell-mediated thermoradiotherapy. Scale bars are represented in the bottom image of each column.

where cells located distal to a functional feeding blood vessel receive insufficient oxygen due to its consumption by the cells closer to the blood vessel. These hypoxic cells maintain their clonogenicity, but their sensitivity to radiation is up to three times less than that of normally oxygenated cells.[26] These radioresistant cells not only contribute to tumor progression but also their location distant from blood flow inevitably means that they have limited access to blood-borne therapeutics. Increasing perfusion via gold nanoshell-mediated hyperthermia, therefore, reduces the fraction of cells within a tumor that are hypoxic and thereby enhances radiation sensitivity.

The second mechanism of observed improvement of efficacy of radiation therapy was due to vascular disruption. Vascular disruption has been proposed as a viable antitumor strategy because damaging a single established blood vessel, via subtle structural changes of dysmorphic endothelial cells or induction of intravascular coagulation, could potentially eliminate hundreds or thousands of tumor cells downstream. Vascular disrupting agents in preclinical and early clinical development include combretastatin A4 phosphate (CA4P), ZD6126, TZT-1027, AVE8062, ABT-751, and MN-029, which target the tubulin cytoskeletal network of endothelial cells, 5,6-dimethylxanthenone-4-acetic acid (DMXAA), which targets autocrine endothelial regulatory cascades, and Exherin (AFH-1), which targets cell adhesion.[27–33] While these agents have shown promise in early trials, there is concern that more than just *tumor* vessels may be targeted by systemic exposure to these agents. In particular, damage to vascular compartments outside the tumor may contribute to acute coronary syndromes and thromboembolic events.[34,35] In contrast to these agents, gold nanoshell-mediated hyperthermia causes vascular disruption that is localized to the tumor, permitting further increase in therapeutic ratio.

The observed radiation dose modification by gold nanoshells is similar to that observed with other forms of hyperthermia. The degree of necrosis observed, however, far exceeds that noted with traditional means of achieving hyperthermia. Notably, this model only evaluates the effects of this combination on single-fraction high-dose radiation therapy, similar to that used in clinical stereotactic radiation therapy applications. Whether the necrosis and consequent hypoxia

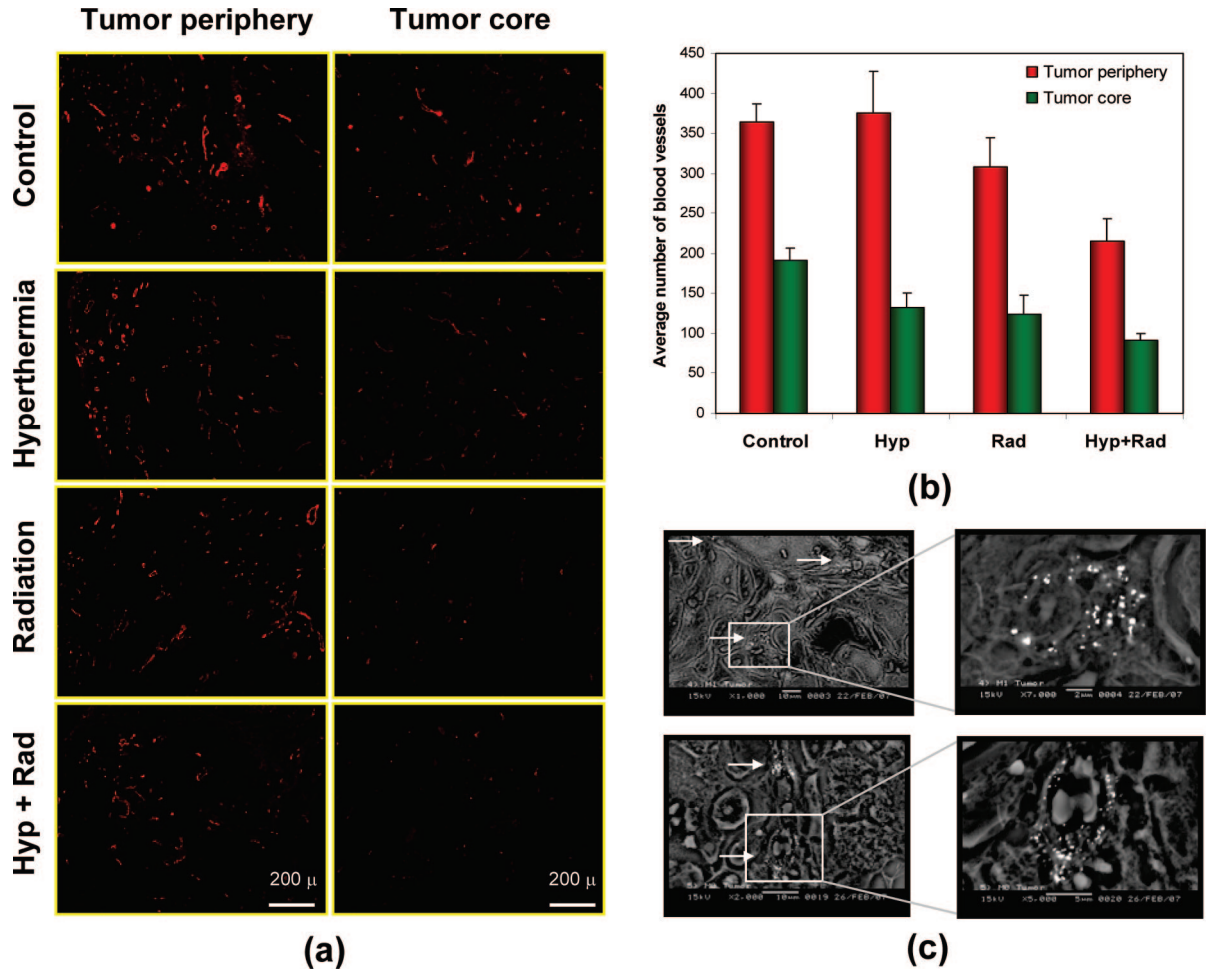

Figure 6. (a) Immunofluorescence staining for the microvessel density in control, hyperthermia, radiation, and thermoradiotherapy treated tumors showing the vessel distribution in tumor periphery (column 1) and tumor center (column 2). (b) Bar chart representing mean ± SE of blood vessels in tumor periphery and tumor core for different treatment groups. (c) SEM images showing the low and high magnification images of gold nanoshell distribution near the perivascular regions in tumors before (row 1: low magnification: 1000×; high magnification: 7000×) and after (row 2: low magnification: 2000×; high magnification: 5000×) gold nanoshell-mediated hyperthermia. The white arrows show the gold nanoshell distribution.

triggered by this combination strategy has a detrimental effect on subsequent fractions of radiation therapy and/or penetrability of subsequent chemotherapy requires continued evaluation. Alternatively, this therapeutic challenge could be converted to an opportunity for targeted therapy using drugs targeting the hypoxia-inducible factor-1 transcription factor, prodrugs activated by hypoxia, hypoxia-specific gene therapy, and recombinant anaerobic bacteria. Alternate sequencing strategies and alterations of the degree of temporal separation between hyperthermia and radiation may be employed to maximize the likelihood that radiation is administered during periods of peak radiosensitivity defined by an optimal tumor oxygenation window or a vascular normalization window.[36,37] Lastly, targeting gold nanoshells to tumor vasculature may further localize and concentrate nanoshells along tumor vasculature to facilitate tumor-directed therapy beyond image-guided physical collimation of the laser beam to the tumor alone. Additional clinical benefit could be realized if substances with a high atomic number (*Z*) accumulate in tissues leading to greater radiation dose deposition, particularly while utilizing kilovolt radiation therapy where highly *Z*-dependent photoelectric interactions are the predominant form of interaction. However, our preliminary calculations, Monte Carlo simulations and in vitro experiments do not bear this out to be a sufficient source of dose escalation to be clinically significant (data not shown). This is likely due to the insufficient tumor parenchymal penetration beyond the immediate perivascular space by the 150 nm nanoshells and the relatively low gold content of each nanoshell in contrast to the significant dose enhancement achievable with smaller nanogold particles.[38]

In summary, this study demonstrates that the gold nanoshell-mediated hyperthermia uniquely enhances the efficacy of radiation therapy by two mechanisms: (1) an early increase in perfusion that reduces the fraction of hypoxic cells that contribute to radiation resistance and (2) a subsequent induction of tumor-specific localized vascular disruption/collapse and extensive necrosis that complements radiation-induced cell death. This study presents a simple means to combine the advantages of two radiation-modifying agents, antiangiogenic agents and vascular disrupting agents, using a single strategy, gold nanoshell-mediated hyperthermia. The

noninvasiveness, minimal/negligible systemic toxicity of gold nanoshells and the promising dual effect of perfusion followed by vascular disruption localized to the tumor observed in this study merits continued evaluation of this therapeutic strategy to improve the therapeutic index of radiation therapy.

Acknowledgment. This work was supported by a seed grant awarded to S.K., J.W.T., J.D.H., and S.H.C. by The University of Texas Center for Biomedical Engineering (UTCBME). This work was also partially supported by the M. D. Anderson Cancer Center support grants P30 CA-16675 and CA16672 for small animal imaging facility and high resolution electron microscopy facility.

Supporting Information Available: Magnetic resonance temperature imaging (MRTI), DCE-MRI, experimental set-up for radiation dose, markers injection, immunofluorescence staining, sample preparation for SEM. This material is available free of charge via the Internet at http://pubs.acs.org.

References

(1) Greish, K. *J. Drug Targeting* **2007**, *15* (7−8), 457–464.
(2) Jain, R. K. *Annu. Rev. Biomed. Eng.* **1999**, *1*, 241–263.
(3) Brigger, I.; Dubernet, C.; Couvreur, P. *Adv. Drug Delivery Rev.* **2002**, *54* (5), 631–651.
(4) Hashizume, H.; Baluk, P.; Morikawa, S.; McLean, J. W.; Thurston, G.; Roberge, S.; Jain, R. K.; McDonald, D. M. *Am. J. Pathol.* **2000**, *156* (4), 1363–1380.
(5) Hirsch, L. R.; Stafford, R. J.; Bankson, J. A.; Sershen, S. R.; Rivera, B.; Price, R. E.; Hazle, J. D.; Halas, N. J.; West, J. L. *Proc. Natl. Acad. Sci. U.S.A.* **2003**, *100* (23), 13549–13554.
(6) O'Neal, D. P.; Hirsch, L. R.; Halas, N. J.; Payne, J. D.; West, J. L. *Cancer Lett.* **2004**, *209* (2), 171–176.
(7) Loo, C.; Hirsch, L.; Lee, M. H.; Chang, E.; West, J.; Halas, N.; Drezek, R. *Opt. Lett.* **2005**, *30* (9), 1012–1014.
(8) Gobin, A. M.; O'Neal, D. P.; Watkins, D. M.; Halas, N. J.; Drezek, R. A.; West, J. L. *Lasers Surg. Med.* **2005**, *37* (2), 123–129.
(9) Agrawal, A.; Huang, S.; Wei Haw Lin, A.; Lee, M. H.; Barton, J. K.; Drezek, R. A.; Pfefer, T. J. *J. Biomed. Opt.* **2006**, *11* (4), 041121.
(10) Su, C. H.; Sheu, H. S.; Lin, C. Y.; Huang, C. C.; Lo, Y. W.; Pu, Y. C.; Weng, J. C.; Shieh, D. B.; Chen, J. H.; Yeh, C. S. *J. Am. Chem. Soc.* **2007**, *129* (7), 2139–2146.
(11) Xie, H.; Gill-Sharp, K. L.; O'Neal, D. P. *Nanomedicine* **2007**, *3* (1), 89–94.
(12) Moeller, B. J.; Richardson, R. A.; Dewhirst, M. W. *Cancer Metastasis Rev.* **2007**, *26* (2), 241–248.
(13) McDonald, D. M.; Choyke, P. L. *Nat. Med.* **2003**, *9* (6), 713–725.
(14) Baluk, P.; Morikawa, S.; Haskell, A.; Mancuso, M.; McDonald, D. M. *Am. J. Pathol.* **2003**, *163* (5), 1801–15.
(15) Harris, A. L. *Nat. Rev. Cancer* **2002**, *2* (1), 38–47.
(16) Hockel, M.; Vaupel, P. *J. Natl. Cancer Inst.* **2001**, *93* (4), 266–276.
(17) Zhang, Y.; Li, M.; Yao, Q.; Chen, C. *Med. Sci. Monit* **2007**, *13* (10), RA175–RA180.
(18) Roti Roti, J. L. *Int. J. Hyperthermia* **2004**, *20* (2), 109–114.
(19) Kampinga, H. H.; Dikomey, E. *Int. J. Radiat. Biol.* **2001**, *77* (4), 399–408.
(20) Horsman, M. R.; Overgaard, J. *Int. J. Hyperthermia* **1997**, *13* (2), 141–147.
(21) Moros, E. G.; Corry, P. M.; Orton, C. G. *Med. Phys.* **2007**, *34* (1), 1–4.
(22) Duff, D. G.; Baiker, A.; Edwards, P. P. *Langumir* **1993**, *9* (9), 2301–2309.
(23) Ishihara, Y.; Calderon, A.; Watanabe, H.; Okamoto, K.; Suzuki, Y.; Kuroda, K.; Suzuki, Y. *Magn. Reson. Med.* **1995**, *34* (6), 814–823.
(24) Jain, P. K.; Lee, K. S.; El-Sayed, I. H.; El-Sayed, M. A. *J. Phys. Chem. B* **2006**, *110* (14), 7238–7248.
(25) Jain, R. K. *Cancer Res.* **1988**, *48* (10), 2641–2658.
(26) Brown, J. M. *Methods Enzymol.* **2007**, *435*, 295–321.
(27) Patterson, D. M.; Rustin, G. J. *Clin. Oncol. (R. Coll. Radiol.)* **2007**, *19* (6), 443–456.
(28) Hinnen, P.; Eskens, F. A. *Br. J. Cancer* **2007**, *96* (8), 1159–1165.
(29) Jameson, M. B.; Baguley, B. C.; Kestell, P.; Zhao, L.; Paxton, J. W.; Thompson, P. I.; Waller, S. *Cancer Chemother. Pharmacol.* **2007**, *59* (5), 681–687.
(30) O'Hanlon, L. H. *J. Natl. Cancer Inst.* **2005**, *97* (17), 1244–1245.
(31) Tozer, G. M.; Kanthou, C.; Baguley, B. C. *Nat. Rev. Cancer* **2005**, *5* (6), 423–435.
(32) Siemann, D. W.; Rojiani, A. M. *Int. J. Radiat. Oncol. Biol. Phys.* **2005**, *62* (3), 846–853.
(33) Siemann, D. W.; Horsman, M. R. *Exp. Rev. Anticancer Ther.* **2004**, *4* (2), 321–327.
(34) van Heeckeren, W. J.; Bhakta, S.; Ortiz, J.; Duerk, J.; Cooney, M. M.; Dowlati, A.; McCrae, K.; Remick, S. C. *J. Clin. Oncol.* **2006**, *24* (10), 1485–1488.
(35) van Heeckeren, W. J.; Sanborn, S. L.; Narayan, A.; Cooney, M. M.; McCrae, K. R.; Schmaier, A. H.; Remick, S. C. *Curr. Opin. Hematol.* **2007**, *14* (5), 468–480.
(36) Dings, R. P.; Loren, M.; Heun, H.; McNiel, E.; Griffioen, A. W.; Mayo, K. H.; Griffin, R. J. *Clin. Cancer Res.* **2007**, *13* (11), 3395–3402.
(37) Winkler, F.; Kozin, S. V.; Tong, R. T.; Chae, S. S.; Booth, M. F.; Garkavtsev, I.; Xu, L.; Hicklin, D. J.; Fukumura, D.; di Tomaso, E.; Munn, L. L.; Jain, R. K. *Cancer Cell* **2004**, *6* (6), 553–563.
(38) Hainfeld, J. F.; Slatkin, D. N.; Smilowitz, H. M. *Phys. Med. Biol.* **2004**, *49* (18), N309–N315.

NL080496Z